PHOTONICS Research

Multiband camouflage design with thermal management

Lehong Huang,[1,2,3,4] Haochuan Li,[1] Zhiguo Li,[1,3,4] Wenbo Zhang,[1,2,3] Caiwen Ma,[1,3,4,5] Chunmin Zhang,[2,6] Yuxuan Wei,[1,3,4] Liang Zhou,[1,4] Xun Li,[1] Zhiyuan Cheng,[1,3,4] Xiaohui Guo,[1] and Shiping Guo[2]

[1]Xi'an Institute of Optics and Precision Mechanics, Chinese Academy of Sciences, Xi'an 710119, China
[2]School of Physics, Xi'an Jiaotong University, Xi'an 710049, China
[3]University of Chinese Academy of Sciences, Beijing 100049, China
[4]Key Laboratory of Space Precision Measurement Technology, Chinese Academy of Sciences, Xi'an 710119, China
[5]e-mail: cwma@opt.ac.cn
[6]e-mail: zcm@xjtu.edu.cn

Received 28 December 2022; revised 22 February 2023; accepted 1 March 2023; posted 3 March 2023 (Doc. ID 484448); published 1 May 2023

Although the effective "stealth" of space vehicles is important, current camouflage designs are inadequate in meeting all application requirements. Here, a multilayer wavelength-selective emitter is demonstrated. It can realize visible light and dual-band mid-infrared camouflage with thermal control management in two application scenarios, with better effect and stronger radiation cooling capability, which can significantly improve the stealth and survivability of space vehicles in different environments. The selective emitter demonstrated in this paper has the advantages of simple structure, scalability, and ease of large-area fabrication, and has made a major breakthrough in driving multiband stealth technology from simulation research to physical verification and even practical application.

https://doi.org/10.1364/PRJ.484448

1. INTRODUCTION

Infrared (IR) signature modulation [1,2] and reflection suppression [3,4] are the main camouflage strategies that reduce the observability of targets in the visible and mid-IR bands. IR camouflage [5–11] is widely used to reduce the thermal radiation energy of various aircraft targets in two atmospheric windows (3–5 and 8–14 μm), thus achieving a stealth effect. According to the Stefan–Boltzmann law, the thermal radiation energy of an object can be suppressed by reducing its emissivity and temperature [12], i.e., reducing radiance $P = \varepsilon\sigma T^4$, where σ is the Stefan–Boltzmann constant, and ε and T are the emissivity and absolute temperature of the object, respectively [13]. As reducing emissivity ε leads to inefficient thermal radiation, the temperature T rises sharply, thus increasing the radiated energy and weakening the stealth performance. To overcome this contradictory behavior, a selective IR stealth material should be designed to achieve low emissivity and thereby low detectability within a specific atmospheric window and high broadband emissivity for adequate radiative cooling in the non-atmospheric window wherein emitted electromagnetic waves cannot be detected owing to attenuation and absorption in the atmosphere. Thus, achieving such multiband camouflage with thermal management has the following requirements: (i) low emissivity in the mid-IR dual band (3–5 μm mid-wavelength IR and 8–14 μm long-wavelength IR); (ii) low reflectance in the visible band; and (iii) high and wide emissivity at 5–8 μm wavelengths for efficient heat dissipation [14–17].

Owing to the different and even conflicting spectral requirements for different wavelength bands, developing multiband mid-IR-compatible camouflage is challenging, and the resulting wavelength-selective emission materials can have broad application prospects in IR stealth technology. However, further research and development in this area are required.

For IR camouflage, structural disguise such as meta surface structures [18–23], insulating metal nanowires [24], core–shell composites [25–27], and thin films (e.g., metal [28] and semiconductor [29,30] films) have been commonly used to reduce the emissivity across the mid-IR band; however, these methods do not achieve satisfactory camouflage effects. Structures that achieve selective IR emission include camouflaged photonic crystals [31–33], resonant metamaterials [34,35], and multilayer films [6,36–39]. Although periodic photonic crystals and resonant metamaterials can be properly tailored to the emissivity of the structure, they are difficult to fabricate and

scale [40–42], whereas multilayer films are easier to implement. The structure of a multilayer film establishes a one-dimensional non-periodic photonic crystal, which can also be considered as a metamaterial. Owing to the increased design freedom realizable with these non-periodic crystals, managing emission and reflection is more efficient than in their periodic counterparts. Recently, Zhu *et al.* [36] designed an IR-selective emitter based on a Ge/ZnS multilayer film and combined it with the thermal-insulating silica aerogel to reduce indoor/outdoor (with/without earthshine) radiation temperature to 310/248 K when observed by an 8–14 μm IR detector at an object temperature of 873/623 K, thus introducing the concept of thermal management. However, this design achieved IR camouflage for a single atmospheric window (8–14 μm) and had a low average emissivity in the non-atmospheric window (5–8 μm) ($\bar{\varepsilon}_{5-8\,\mu m} = 0.58$), resulting in limited radiative cooling capability. Wang *et al.* [39] proposed an infrared-selective generator based on a $Ge/TiO_2/SiO_2$ multilayer film, which could achieve two atmospheric windows with low-emissivity mid-infrared camouflage and non-atmospheric windows with high-emissivity radiation cooling through simulation analysis. However, the design had only two stealth bands, which is a small number, and only simulation analysis had been performed; a physical object was not prepared for experimental verification, as it is known that experimental verification results can better demonstrate the authenticity of the design results. It is difficult to prepare the physical multilayer film, which must consider the bonding between different materials and the setting of processing parameters, etc., since TiO_2 is a medium refractive index material. To improve the infrared-selective emissivity, the design adds SiO_2; however, using one more material will cause the structure to become complicated and the cost to rise. SiO_2 has weak absorption in the 5–14 μm band, which will reduce the infrared-selective emissivity in the 5–8 μm non-atmospheric window and the 8–14 μm atmospheric window, and the simulation results are not outstanding. In summary, previous research faced problems such as low number of stealth bands, narrow stealth spectral range, and difficulty with regard to practical application. In addition, multiband stealth technology, which is a cutting-edge emerging technology, has not been studied considerably, and most of those studies were based on simulation, with very little physical verification.

We select two common high-temperature-resistant materials, Ge and YbF_3, to develop a multilayer wavelength-selective emitter that can achieve visible and dual-band mid-infrared camouflage with thermal control management in two different application scenarios. Compared with previous studies, more wavelengths for camouflage are covered, and two infrared wavelengths show lower emissivity for better camouflage. In addition, higher emissivity for non-atmospheric window wavelengths and better radiation cooling can be achieved. The knot of the simulation analysis is significantly better than that in the previous simulation by Wang *et al.* [39]. YbF_3 provides a lower refractive index than common low-refractive-index optical film materials, such as ZnS, in the infrared band. The contrast of YbF_3 is further increased by the high-refractive-index Ge to achieve better camouflage and theoretical performance. For the membrane structure, we combine the transfer matrix method and particle swarm optimization such that the structure mitigates wave band artifacts through multiple iterations. For the multilayer films, as the binding of YbF_3 to Ge is weaker than that of ZnS to Ge, the process technology for film preparation is more demanding. Hence, we use electron beam evaporation for deposition coating and tune the coating parameters to produce optimal Ge/YbF_3 multilayer films.

The proposed wavelength-selective emitter demonstrates multiband camouflage with thermal control management in two scenarios. For the first application, the selective emitter is used as the aircraft skin coating for dual-band IR camouflage (low emissivity in the atmospheric windows, $\bar{\varepsilon}_{3-5\,\mu m} = 0.06$ and $\bar{\varepsilon}_{8-14\,\mu m} = 0.01$) and radiative cooling (high emissivity in the non-atmospheric window, $\bar{\varepsilon}_{5-8\,\mu m} = 0.68$) as well as visual camouflage (low average reflectivity of 0.21 in the visible band). In addition, selective IR emission is maintained for incidence angles of radiated light between 0° and 60°. For the second application, a multilayer wavelength-selective emitter is combined with a thermal insulation material (silica aerogel) in the converging nozzle of an aircraft, which reduces the apparent temperature of a hot object. For instance, when the object temperature is 873 K, the radiation temperature can be reduced to 314/313 K as recorded by 3–5/8–14 μm detectors indoors at daytime (with earthshine) and to 311/310 K outdoors at nighttime (without earthshine). Compared with no camouflage, the locking range at which radiation from hot objects is detected is reduced by approximately 79%. The electron beam evaporation deposition coating process we use usually uses a rotating substrate or multiple evaporation sources to achieve large-area coating, and it is easy to ensure the uniformity of the large-area film layer, and the uniformity of the film layer can ensure the selective emission characteristics. If the single crystal silicon of the substrate is replaced by the flexible material polyimide, a selective emitter with ductility can be made.

We validated the two applications through simulations based on a finite-difference time-domain approach and experiments. Overall, the applications demonstrate the following advantages.

(i) The simple photonic structure enables efficient multiband camouflage (for both visible and dual-band IR) and thermal control management, as well as the ability to continuously camouflage targets over a large field of viewing angles.
(ii) Compatibility of thermal management (requires high emissivity) and IR camouflage (requires low emissivity).
(iii) For radiative cooling, the photonic structure is able to reduce the surface temperature of the object significantly—more than a dozen degrees lower than conventional IR camouflage materials.
(iv) Simple structure, easy processing, high realizability, and being suitable for mass production.

2. RESULTS

Multilayer film structures provide adequate spectral selectivity and are easy to prepare. We used two common high-temperature-resistant materials, Ge and YbF_3, to form a coating and designed a wavelength-selective IR emitter that provides visible-band camouflage, IR-band camouflage, and

heat dissipation. In IR optical coatings, YbF_3 is a commonly used low refractive index material because of its useful IR transmission properties and high layer strength. YbF_3 is widely used to coat germanium and sulfur IR glass with a transmission-enhancement film. Germanium is also commonly used and is a stable IR material, with a refractive index above four, reaching a reflection loss of more than 50%. Using a transmission-enhancement film, the transmission rate of germanium can be significantly increased up to 98% or more. The large refractive index contrast and difference in absorption regions become the basis for strong interference and selective absorption.

Wavelength-selective emitters were prepared by depositing alternating Ge and YbF_3 multilayer films on thin silica substrates. By combining the transfer matrix method with particle swarm optimization, a 14-layer film structure was designed with low emissivity in the two main bands of IR detection ($\bar{\varepsilon}_{3-5\,\mu m} = 0.06$ and $\bar{\varepsilon}_{8-14\,\mu m} = 0.01$) and high emissivity in the intermediate band ($\bar{\varepsilon}_{5-8\,\mu m} = 0.68$). Concurrently, the wavelength-selective emitter shows low reflectivity in the visible band (average reflectivity of 0.21). The conceptual characteristics of the designed structure are graphically depicted in the aircraft skin and converging nozzle shown in Fig. 1.

The first application was based on a coated aircraft surface, where visible and IR detection was avoided by reducing the reflectivity in the visible band and emissivity within the atmospheric window spectrum (i.e., 380–780 nm, 3–5 μm, and 8–14 μm wavelengths). Conversely, increasing the high broadband emissivity outside the atmospheric window (5–8 μm) facilitated heat dissipation to cool the surface and attenuate thermal emission on the detection spectrum by reducing the surface temperature and avoiding thermal instability.

The second application considered the aircraft converging nozzle. The corresponding high-temperature IR camouflage was combined with a thermal insulator and wavelength-selective emitter. Owing to the high observability in the visible band of the wake flame, visual camouflage was not considered for this application. The insulator was fixed directly to the high-temperature converging nozzle, and the designed emitter was placed on top of the insulator. The insulator was a commercially available high-emissivity silica aerogel blanket, which has a long-term temperature resistance of up to 923 K [43]. Combining wavelength-selective emitters with thermal insulation can significantly increase the temperature range of high-temperature IR camouflage [36].

Overall, the demonstrated applications can contribute to the design of aircraft coatings that combine thermal management and multiwavelength camouflage.

A. Structural Design and Measurement

We applied particle swarm optimization [44] and the transfer matrix method to optimize parameters including the number of layers and thickness to obtain the desired emission spectrum for the multilayer film structure. Particle swarm optimization performs stochastic search based on group collaboration by mirroring the foraging behavior of flocks of birds, thus enabling highly non-linear and stochastic optimization. This optimization approach differs from conventional optimization because it acts on the entire space simultaneously and, thus, efficiently leads to reliable solutions. Conversely, the widely used transfer matrix method has been theoretically and experimentally demonstrated in the design of multilayer structures.

First, we applied the transfer matrix method to describe the optical properties of the structure and then added an optimization function for particle swarm optimization. We defined a value function that represents the residual error between the emissivity spectrum of a given structure and the target spectrum to minimize the cost function toward the desired emission spectrum. As we also considered low reflection in the visible band, the film structure was reflective, and the full-band target parameter was reflectance $R(\lambda)$. Thus, the optimization function was defined as follows:

$$F(n,d) = \min_R \frac{1}{2}\sum_{\lambda} W(\lambda)[R(\lambda;n,d) - R^*(\lambda)]^2, \quad (1)$$

where n is the number of film layers; d is the thickness of each layer; $W(\lambda)$ is the weight of each frequency band, which was set to $W(\lambda_{0.3-0.8\,\mu m}):W(\lambda_{0.8-3\,\mu m}):W(\lambda_{3-5\,\mu m}):W(\lambda_{5-8\,\mu m}):W(\lambda_{8-14\,\mu m}) = 1:1/3:1:1:1$; $R^*(\lambda)$ is the objective function, i.e., the most desirable emission spectrum with the expected value of $R(\lambda_{0.3-0.8\,\mu m}) = 0$, $R(\lambda_{0.8-3\,\mu m}) = 0$, $R(\lambda_{3-5\,\mu m}) = 1$, $R(\lambda_{5-8\,\mu m}) = 0$, $R(\lambda_{8-14\,\mu m}) = 1$; and $R(\lambda;n,d)$ is the emissivity of the normal spectrum of the multilayer film calculated by the transmission matrix method. The particle update for optimization was given by

$$X_i(t+1) = X_i(t) + c_1 r_1[P_i(t) - X_i(t)] + c_2 r_2[P_g(t) - X_i(t)], \quad (2)$$

where X is the particle position, r_1 and r_2 are random numbers in [0,1], i indicates the current iteration, $P_i(t)$ is the individual optimal particle position, $P_g(t)$ is the global optimal particle position, and c_1 and c_2 are learning factors ($c_1 = c_2 = 2$ in this study).

Particle swarm optimization iteratively processed 91 generations. After completing optimization, the best multilayer film structure (i.e., wavelength-selective emitter) was obtained, as shown in Fig. 2(a). The multilayer film was formed by the alternate deposition of 14 layers of Ge and YbF_3. The film parameters are listed in Table 1, and the emissivity spectrum of the emitter is shown in Fig. 2(c), exhibiting excellent wavelength-selective emission performance in the IR range.

Titanium alloy TC4 has low surface emissivity and is being widely used for military targets. We use this alloy as a low-emissivity reference. Compared with TC4 without wavelength-selective radiation, the proposed emitter had a much greater emissivity in 5–8 μm and a smaller emissivity in 3–5 and 8–14 μm, as shown in Fig. 2(c). In addition, our emitter showed low reflectivity in the visible band of 380–780 nm, with an average reflectivity of 0.21 [Fig. 2(d)], enabling visible-band camouflage of the aircraft surface. The visible light camouflage in this paper is for visible light detectors. Reducing the target reflectivity is equivalent to reducing the brightness of the reflected light irradiation of the target, thus reducing the range in which the target can be detected, and thus achieving stealth [45].

The difference between simulated and measured emissivity/reflectivity is attributed to errors during coating deposition.

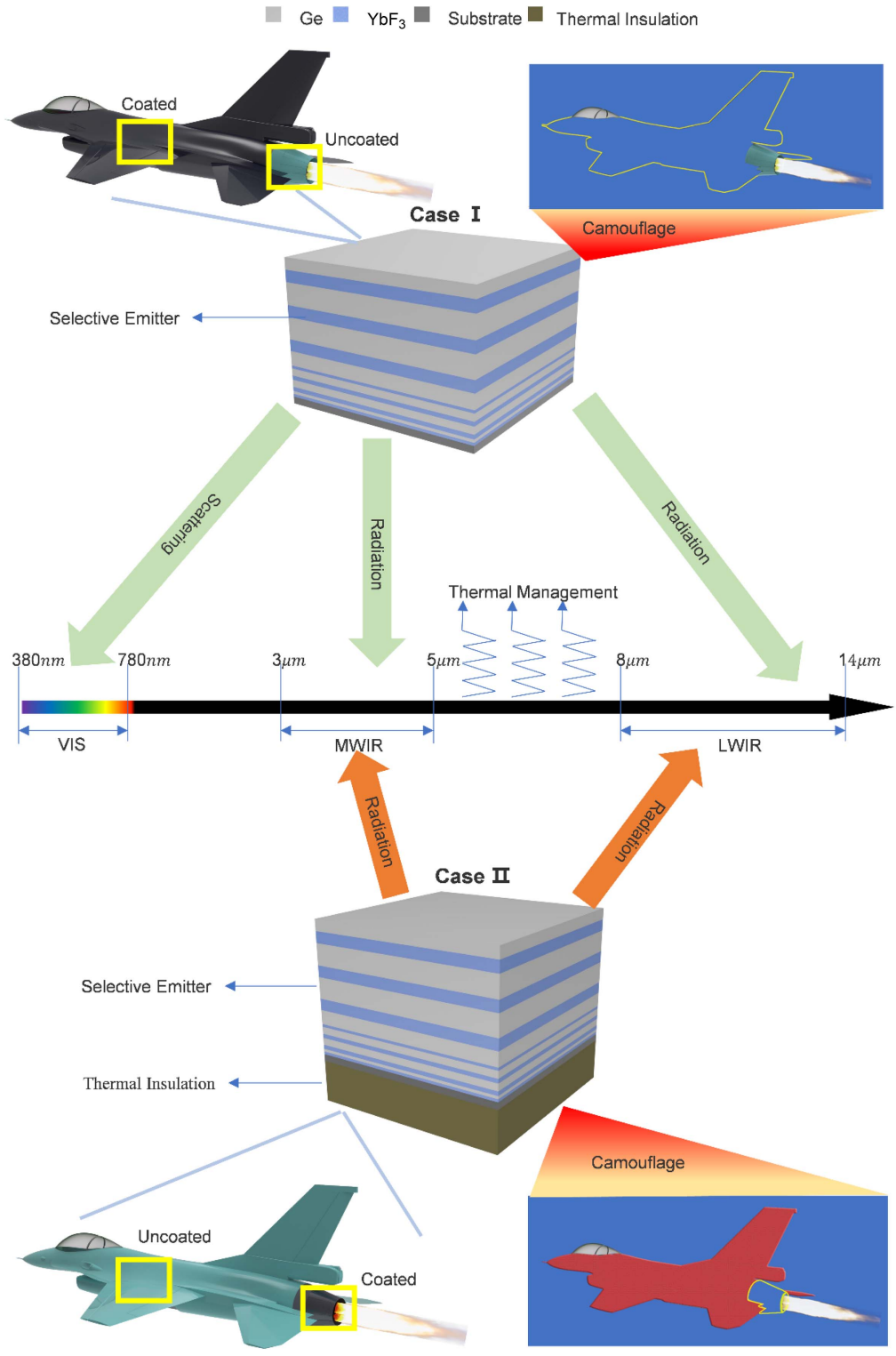

Fig. 1. Schematic of simultaneous multiband camouflage and thermal management in aircraft. Case I. Wavelength-selective emitter with multilayer film structure enables multiband camouflage and thermal management of the aircraft skin. Case II. Emitter combined with thermal insulation enables multiband mid-IR camouflage and thermal management of the aircraft converging nozzle.

We observed the flatness of the film with a laser confocal microscope, and there were some tiny pores on the surface of the film, which revealed the processing errors generated by the electron beam evaporation coating.

B. Finite-Difference Time-Domain Simulation Analysis

We simulated and calculated the average emissivity for each spectral range at different temperature conditions using the

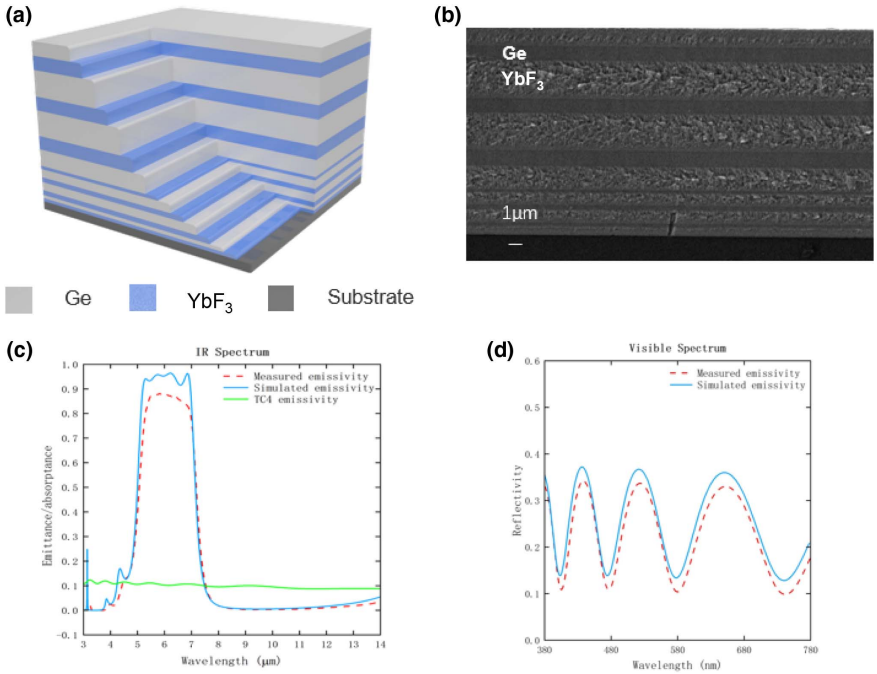

Fig. 2. Simulation and measurements of multilayer film structure. (a) Schematic of the film cladding structure. (b) Scanning electron microscopy image of the prepared Ge/YbF_3 multilayer film (14 layers) at a scale of 1 μm. (c) Simulated emission/absorption spectra of selected emitters (blue solid line), emission/absorption spectra of selected emitters measured by Fourier-transform IR spectroscopy (red dashed line), and comparison with measured titanium alloy TC4 emission/absorption spectra. (d) Simulated reflectance in the visible band of the wavelength-selective emitter (blue solid line) and reflectance measured by the spectrophotometer (red dashed line).

Table 1. Number of Layers and Thickness of Film Obtained from Particle Swarm Optimization

Layer	1	2	3	4	5	6	7	8	9	10	11	12	13	14
Material	Ge	YbF_3	Ge	YbF_3	Ge	YbF_3	Ge	YbF_3	Ge	YbF_3	Ge	YbF_3	Ge	YbF_3
Thickness (nm)	87.74	244.66	151.48	507.43	194.96	523.93	117.91	957.00	681.59	1507.15	611.67	1564.57	621.93	724.46

finite difference time domain method. This method enables us to quantitatively show the infrared artifact and heat dissipation performance of the designed film system, as detailed in Fig. 2(c). Average emissivity ε between wavelengths λ_1 and λ_2 of a material can be obtained by

$$\varepsilon[\lambda_1, \lambda_2]_{\text{avg}} = \int_{\lambda_1}^{\lambda_2} \frac{\varepsilon(\lambda) I_{\text{BB}}(\lambda, T)\mathrm{d}\lambda}{\int_{\lambda_1}^{\lambda_2} I_{\text{BB}}(\lambda, T)\mathrm{d}\lambda}. \tag{3}$$

According to Planck's law, $I_{\text{BB}}(\lambda, T) = (2hc^2/\lambda^5) \cdot [\exp(\frac{hc}{\lambda k_B T}) - 1]^{-1}$ is the radiation energy of a blackbody at wavelength λ and temperature T. $\varepsilon(\lambda)$ is the film normal spectral emissivity.

Considering the wide temperature range on the aircraft surface, we simulated temperatures between 300 and 1000 K. The designed film achieved near-ideal IR-selective emission; the emissivity was below 0.15 in 3–5 μm wavelength range and below 0.05 in 8–14 μm, and a high emissivity occurred in 5–8 μm. There was a significant change in the spectral emissivity at the boundary in 5–8 μm. With increasing temperature, the average emissivity in 3–5 and 8–14 μm fluctuated slightly around 0.06 and 0.01, respectively. The fluctuation in the 5–8 μm range was high, with an average emissivity in 5–7 μm being 0.96; the peak of the object radiant energy blue-shifted to a shorter wavelength with increasing temperature while the average emissivity may slightly vary depending on the spectral emissivity distribution in each range. The simulation results indicated that the selective emitter provided high-performance mid-IR camouflage and thermal management in the temperature range 300–1000 K.

The mechanism of selective infrared emission from multilayer membrane structures can be well understood by analyzing the radiant energy transport distribution at different wavelengths within each layer of the multilayer membrane. Therefore, we used the finite difference time domain method to solve Maxwell's equations and calculated the radiant energy transport distribution [46]. For example, the distributions of the electric field intensity and Poynting vector space perpendicular to the film surface were calculated in three band ranges of 3–5, 5–8, and 8–14 μm at wavelengths of 3.5, 5.8, and 9.2 μm, respectively (results shown in Fig. 3). In the layers with wavelengths of 3.5 and 9.2 μm, most of the energy was concentrated on the outer surface of the film, while the energy decreased sharply on its inner surface and high

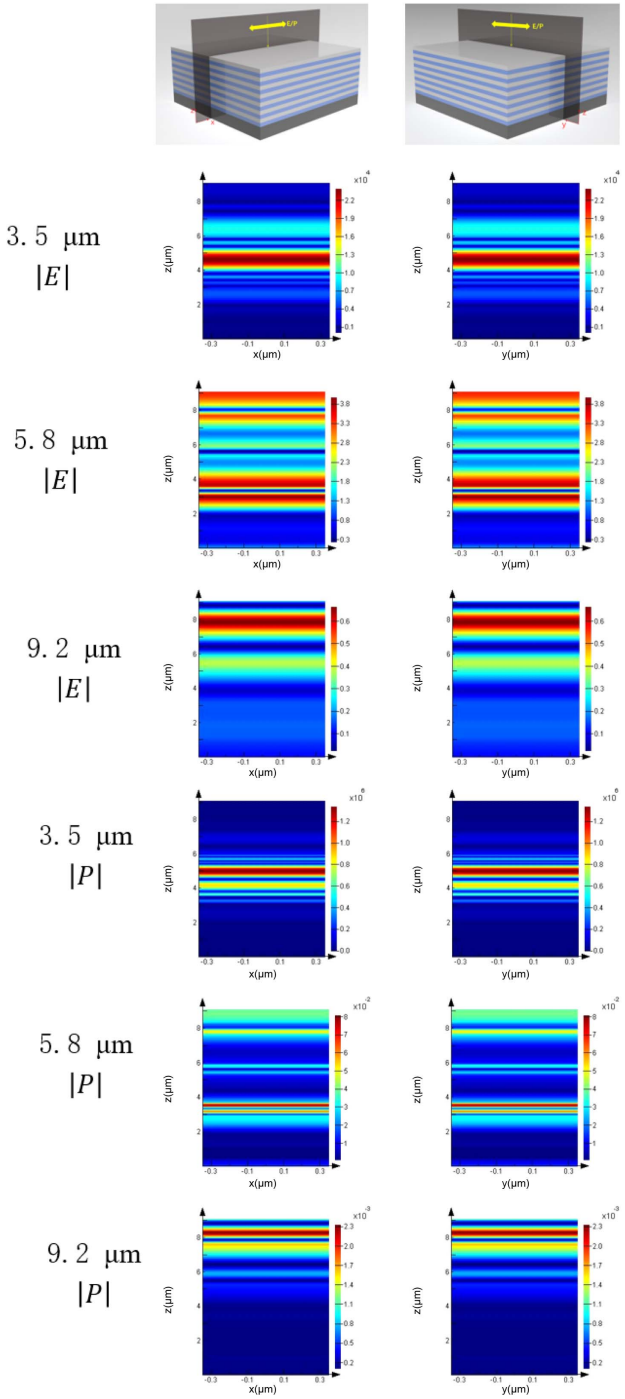

Fig. 3. Schematic of the selective IR emission mechanism of the multilayer film structure. Electric field intensity (E) and Poynting vector (P) of the wavelength-selective emitter on the XZ and YZ cross sections at wavelengths of 3.5, 5.8, and 9.2 μm.

resonance appeared only near the surface of the film structure. The highly reflective property of the film structure enabled IR artefacts to be achieved between the two wavelengths. In contrast, at 5.8 μm, the radiated energy was transmitted for a long time within the film and penetrated the structure, transferring most of the energy to the substrate, which indicates large absorption by the substrate facilitating heat dissipation.

In many applications, both transverse electric and magnetic waves require emission over large incidence angles. Figures 4(a) and 4(b) show the emissivity according to the wavelength for transverse electric and magnetic polarized waves at oblique incidence angles (different colored lines). As the incidence angle increased, the overall high emission band of the transverse magnetic wave blueshifted with an almost constant bandwidth. Although the bandwidth of the high-emission band of the transverse electric wave decreased, the entire emission spectrum maintained high performance. In addition, the emission band did not deviate from 5–8 μm for incidence angles up to 60°, as shown in Fig. 4(c). Hence, the designed film structure could operate over a wide range of incidence angles.

C. IR Camouflage Evaluation

We characterized the IR stealth performance of the wavelength-selective emitter based on thermal radiation properties in two atmospheric windows and evaluated it against the performance of a low-emissivity titanium alloy as a reference.

When the IR detector was located below the aircraft, the detector collected radiation from both the aircraft and reflected earthshine, as shown in Fig. 5(a). To simulate this scenario, we performed measurements indoors, collecting both the radiation emitted and ambient radiation reflected by the sample. To simulate practical application and demonstrate the reduction in apparent temperature and IR camouflage performance of the high-temperature object, we placed the wavelength-selective emitter (sample I) and titanium alloy (sample II) on the high-temperature object at a background temperature of 373 K. The apparent temperatures of samples I and II were measured, and IR images were captured in two atmospheric windows. To simulate the thermal management application, we placed the wavelength-selective emitter on silica aerogel to form sample III, titanium alloy on silica aerogel to form sample IV, and a blanket of silica aerogel to form sample V. At a background temperature of 873 K, we measured the apparent temperatures of samples III–V in two atmospheric windows and captured IR images. The corresponding IR images are shown in Fig. 6, and the apparent temperatures, T, of samples I–V are shown in Fig. 7.

IR camouflage performance was obtained by inferring the surface temperature of a sample from the IR power detected. The temperature measured by the mid-IR detector, called radiation temperature T_r, is the inverse of relation $P(\epsilon, T)$ between the IR light intensity and temperature:

$$T_r = P^{-1}(\epsilon_{\mathrm{IR}}, T), \tag{4}$$

where ϵ_{IR} is the default emissivity built into the IR detector (usually $\epsilon_{\mathrm{IR}} = 1$). $P(\epsilon, T)$ represents the radiation intensity detected from the object surface, which includes the true radiation intensity of the sample surface (P_{rad}) and ambient radiation intensity reflected by the object (P_{ref}):

$$\begin{aligned} P(\epsilon, T) &= P_{\mathrm{rad}}(\epsilon, T) + P_{\mathrm{ref}}(\epsilon, \epsilon_a, T_a) \\ &= C\int_{\lambda_1}^{\lambda_2} \epsilon(\lambda) I_{BB}(\lambda, T)\mathrm{d}\lambda \\ &\quad + C\int_{\lambda_1}^{\lambda_2} [1-\epsilon(\lambda)]\cdot\epsilon_a(\lambda)\cdot I_{BB}(\lambda, T_a)\mathrm{d}\lambda, \end{aligned} \tag{5}$$

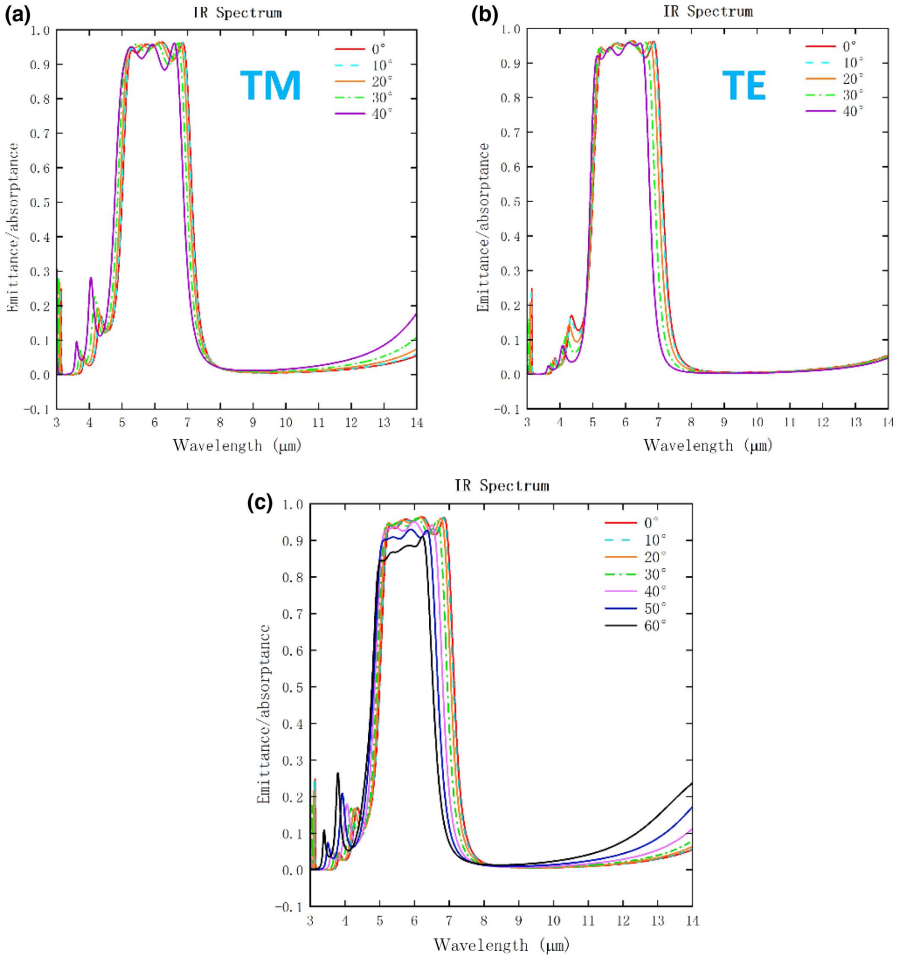

Fig. 4. (a), (b) Emissivity versus wavelength for transverse electric and magnetic polarized waves at oblique incidence angles 0°–40°. (c) For a gradual increase in the incidence angle from 0° to 60°, although the emissivity gradually decreases, the emission band does not deviate from 5–8 μm.

where $\epsilon(\lambda)$ and $\epsilon_a(\lambda)$ are the radiation spectra of the sample and environment, respectively, T is the surface temperature of the sample, T_a is the ambient temperature, $[\lambda_1, \lambda_2]$ is the detection band of the IR camera, and C is an angular integration constant that does not influence the results given by the automatic calibration of the IR camera.

Under IR detector observations in the 3–5 μm range, the average apparent temperature of the wavelength-selective emitter was lower than that of the reference titanium alloy. Although the emitter and titanium alloy had similar emissivity in this band, the lower true temperature of the emitter was caused by radiative cooling. At a background temperature of 373 K, the difference in apparent temperature between samples I and II was 10.9°C. Owing to the excellent insulation of the aerogel blanket, its apparent temperature (410 K) was significantly lower than the background temperature of 873 K, with a difference in apparent temperature between samples III and IV being 10.2°C. Similar experimental results were observed with an IR detector in the 8–14 μm range. At a background temperature of 373 K, the difference in apparent temperature between samples I and II was 13.3°C, and at a background temperature of 873 K, the difference between samples III and IV was 11.3°C.

For an IR detector installed above the aircraft, no reflected earthshine was involved, as shown in Fig. 5(b), and the IR detector only collected radiation from the object. To simulate this scenario, we conducted outdoor experiments on a clear night. At a background temperature of 373 K, the difference in apparent temperature between samples I and II was 12.5°C when observed with an IR detector in the 3–5 μm range and 15.6°C in the 8–14 μm range. At a background temperature of 873 K and a silica aerogel surface temperature of 405 K, the difference in apparent temperature between samples III and IV was 11.3°C when observed with an IR detector in the 3–5 μm range and 12.2°C in the 8–14 μm range.

Overall, we could achieve IR camouflage by designing wavelength-selective emitting materials to reduce the apparent temperature in the atmospheric window and modulate the thermal radiation properties. Depending on the net radiation flux, the wavelength-selective emitter was designed to have a higher thermal emissivity than the reference, thereby achieving a higher radiative cooling efficiency and lower actual temperature.

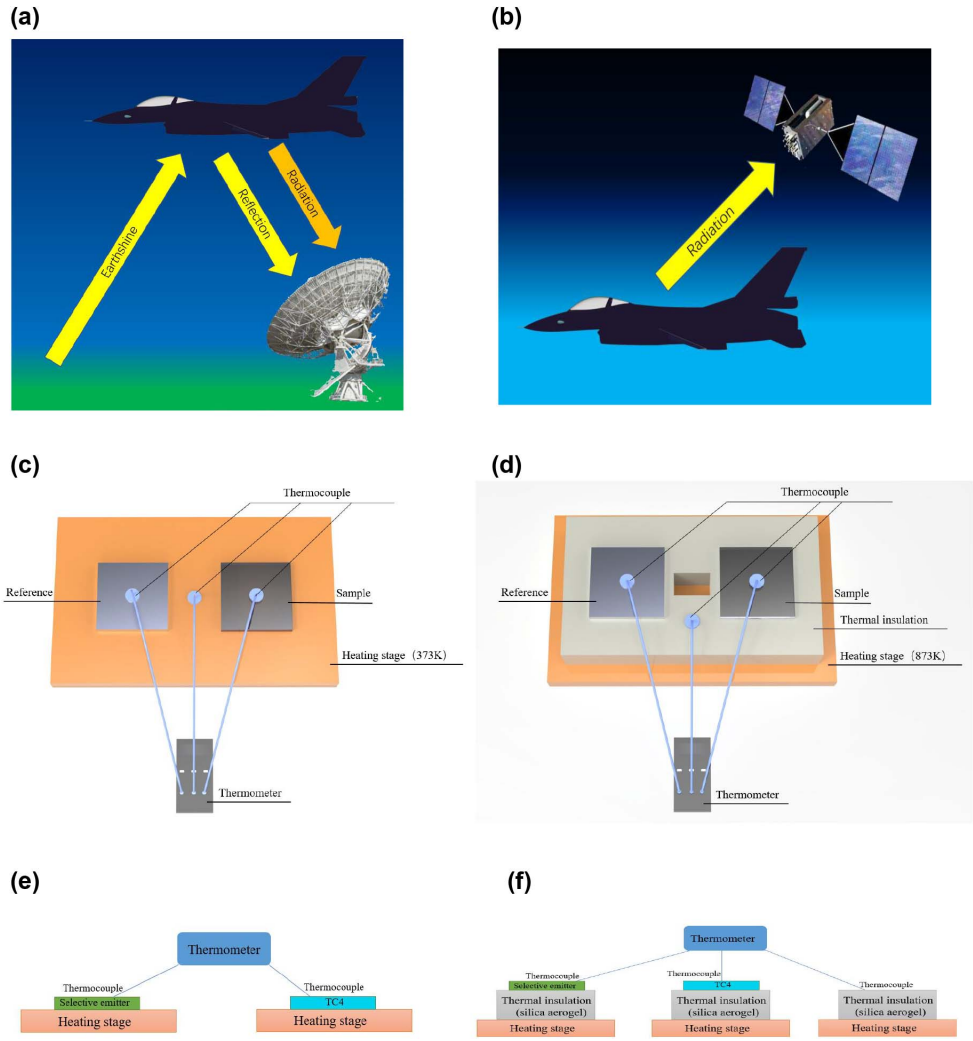

Fig. 5. Diagram of the IR camouflage scheme. (a), (b) Schematic of radiation reflection detection with and without earthshine. (c), (d) Schematic of experimental setup for thermal measurement of radiation cooling performance at background temperatures of 373 and 873 K. (e), (f) Experimental samples at two background temperatures. Samples I and II are directly heated wavelength-selective emitters and titanium alloy references, respectively, and samples III–V are wavelength-selective emitter on aerogel, titanium alloy on aerogel, and bare aerogel, respectively.

The theoretical maximum difference in emissivity between the wavelength-selective emitter and reference occurred mainly in the 5–8 μm range rather than in the atmospheric window. The level of radiation flux in 5–8 μm was positively correlated with emissivity, and differences in emissivity led to differences in the net radiation flux and a greater difference in the thermal cooling capacity. In contrast, the emissivity of the wavelength-selective emitter and titanium alloy reference were similar within the two atmospheric windows, and the thermal radiation had a lower effect on the net radiation flux. Thus, the wavelength-selective emitter had a greater ability than the reference to dissipate heat in the non-atmospheric window.

We experimentally verified that the selective emitter was temperature tolerant because the emission spectra of the Ge/YbF_3 multilayer film remained almost unchanged before and after heating at 573 K for 1 h (see Appendix B). The lack of delamination after heating at 573 K for 1 h also demonstrated the robustness of the designed wavelength-selective emitter film.

To quantitatively assess the IR camouflage performance, we introduce the metric lock-on range, which is related to the radiation intensity of an object and reflected earthshine radiation [47]. An object can only be detected if the range between the object and detector is within the lock-on range. Therefore, a smaller lock-on range indicates stronger IR camouflage. The lock-on range is determined by the sensitivity and irradiance of the IR detector, which are related to the radiation intensity of the object and reflected earthshine radiation. The lock-on range is calculated in the 3–5 μm ($R_{LO,3–5}$) and 8–14 μm ($R_{LO,8–14}$) ranges as follows:

$$R_{LO,3–5} = \sqrt{\frac{A_{obj} H_{3–5}}{\Omega_{obj} \cdot NEI \cdot \xi_{min}}}, \tag{6}$$

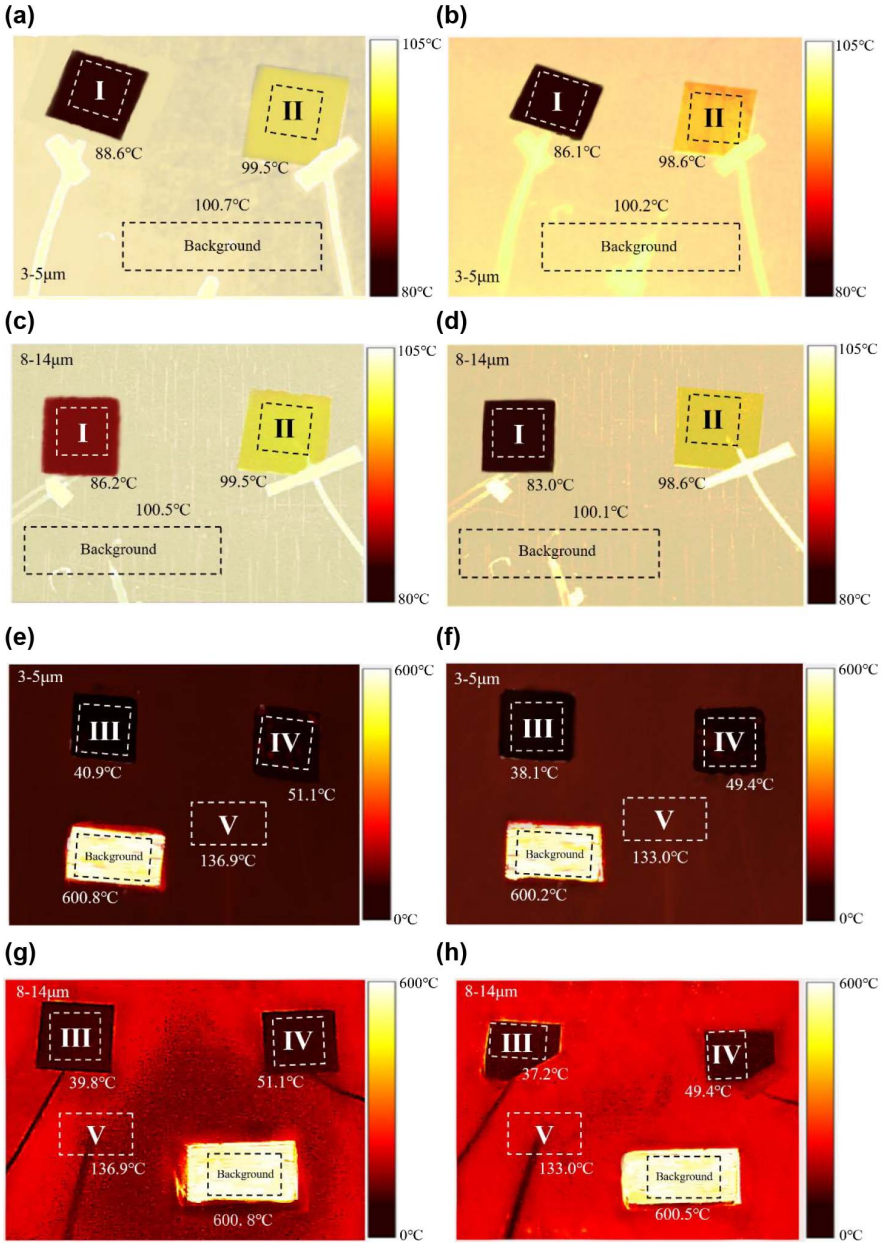

Fig. 6. Apparent temperature and thermal IR images (steady state) of different slices. (a), (b) Thermal IR image captured by the detector with a background temperature of 373 K at daytime/nighttime for the 3–5 μm range. The wavelength-selective emitter is sample I and the titanium alloy reference is sample II. (c), (d) Thermal IR image captured by the detector with a background temperature of 373 K at daytime/nighttime for the 8–14 μm range. (e), (f) Thermal IR image captured by the detector with a background temperature of 873 K at daytime/nighttime for the 3–5 μm range. The wavelength-selective emitter is sample III, the titanium alloy reference is sample IV, and the silica aerogel is sample V. (g), (h) Thermal IR image captured by the detector with a background temperature of 873 K at daytime/nighttime for the 8–14 μm range.

$$H_{3\text{–}5} = \Omega_{\text{obj}} \cdot \int_{3\ \mu\text{m}}^{5\ \mu\text{m}} \varepsilon(\lambda) M_{\text{bb}}(\lambda, T_{\text{obj}}) \tau_{\text{atm}}(\lambda) + [1 - \varepsilon(\lambda)] M_{\text{bb}}(\lambda, T_{\text{ear}}) \tau_{\text{atm}}(\lambda) \mathrm{d}\lambda, \tag{7}$$

$$R_{\text{LO},8\text{–}14} = \sqrt{\frac{A_{\text{obj}} H_{8\text{–}14}}{\Omega_{\text{obj}} \cdot \text{NEI} \cdot \xi_{\text{min}}}}, \tag{8}$$

$$H_{8\text{–}14} = \Omega_{\text{obj}} \cdot \int_{8\ \mu\text{m}}^{14\ \mu\text{m}} \varepsilon(\lambda) M_{\text{bb}}(\lambda, T_{\text{obj}}) \tau_{\text{atm}}(\lambda) + [1 - \varepsilon(\lambda)] M_{\text{bb}}(\lambda, T_{\text{ear}}) \tau_{\text{atm}}(\lambda) \mathrm{d}\lambda, \tag{9}$$

where $H_{3\text{–}5}$ and $H_{8\text{–}14}$ are the band-integrated irradiance values on the IR detector calculated from object surface emissivity $\varepsilon(\lambda)$, blackbody spectral radiance M_{bb} at object surface temperature T_{obj} and ground temperature T_{ear}, atmospheric transmission spectrum $\tau_{\text{atm}}(\lambda)$, and object effective angle Ω_{obj}. Lock-on ranges are obtained using the minimum threshold of the IR

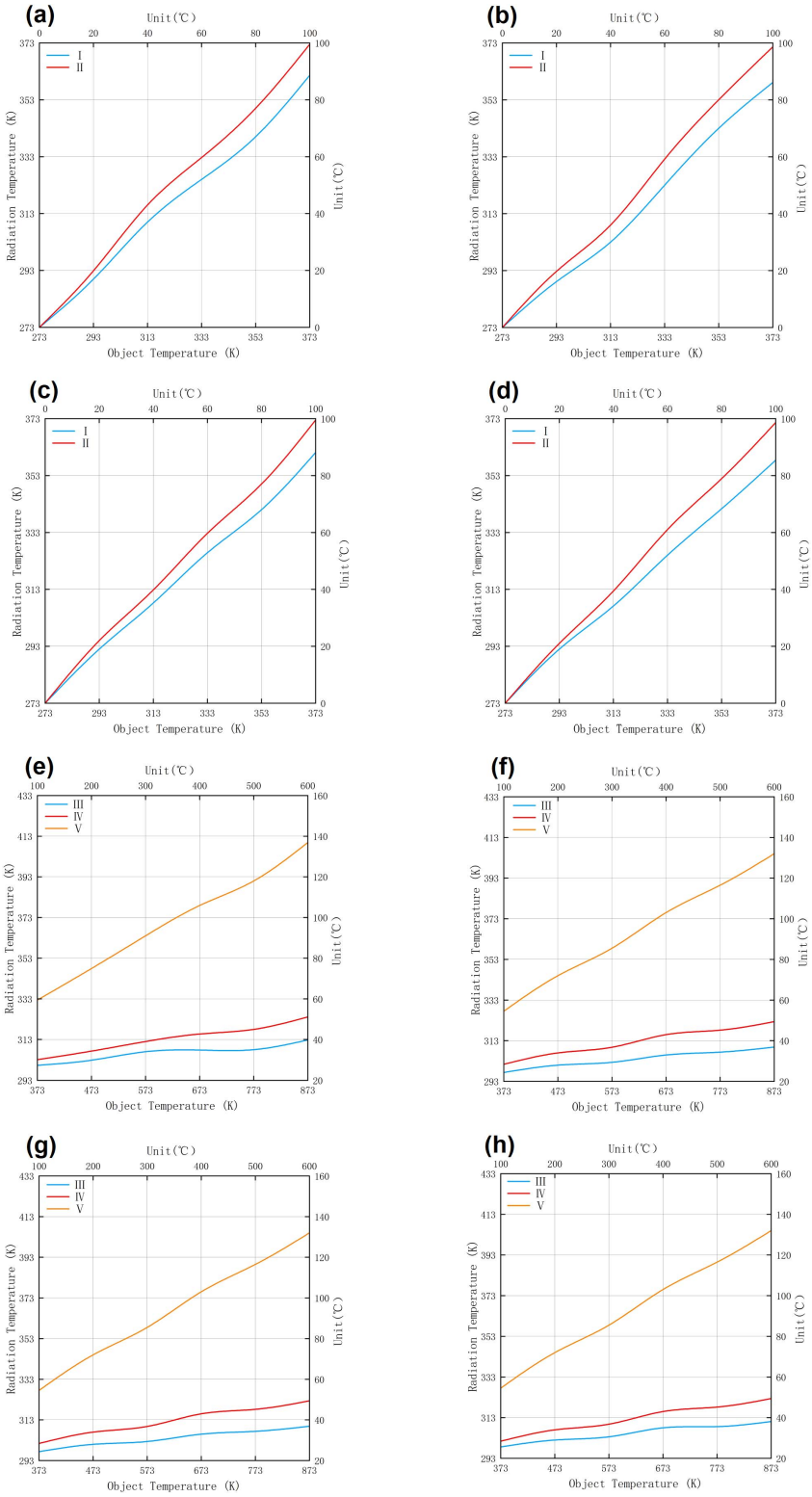

Fig. 7. Apparent temperature change with increasing temperature for different samples. (a), (b) Apparent temperature change measured at 373 K background temperature using a 3–5 μm detector at daytime/nighttime. (c), (d) Apparent temperature change measured at 373 K background temperature using a 8–14 μm detector at daytime/nighttime. (e), (f) Apparent temperature change measured at 873 K background temperature using a 3–5 μm detector at daytime/nighttime. (g), (h) Apparent temperature change measured at 873 K background temperature using a 8–14 μm detector at daytime/nighttime.

detector (NEI · ξ_{min}), effective area of the target A_{obj}, effective angle of the object, Ω_{obj}, and irradiance values H_{3-5} and H_{8-14}.

As the total radiation incident on the IR detector is the sum of the aircraft skin, plume, and exhaust radiations, we conducted simulations using a temperature of 837 K for the application of thermal management which took into account the three types of radiations. In the 3–5 μm range, sample III showed a 77.9% reduction in the lock-on range compared with no artifacts under the same conditions (with and without earthshine). In the 8–14 μm range, sample III showed an 80.1% reduction in the lock-on range under the same conditions (with and without earthshine) compared with no camouflage.

The experiments demonstrated that samples I and III can further suppress thermal radiation in the atmospheric window by combining reduced emissivity and active radiative cooling, thus providing enhanced IR camouflage compared with conventional low-emissivity materials. Overall, wavelength-selective emissive materials have promising application prospects in IR stealth technology.

3. DISCUSSION AND CONCLUSION

We propose a multiwavelength camouflage design with thermal management evaluated in two application scenarios. The proposed wavelength-selective emitter design is integrated into aircraft surface coating and simultaneously achieves a stealth effect and thermal management in the visible and two IR bands (3–5 and 8–14 μm). Thus, the emitter resolves the conflicting low IR emissivity required for IR camouflage and high IR emissivity required for thermal management. The selective IR emission characteristics are virtually consistent over surface temperatures in the range 300–1000 K and over incidence angles of radiated light from 0° to 60°, providing a wide range for IR camouflage. Two commonly used high-temperature-resistant materials, Ge and YbF_3, and conventional electron-beam evaporation deposition coating are applied in this design, leading to a simple structure, convenient manufacturing, and wide application prospects. Overall, we explore the proposed simple structural design to achieve coordinated control of multiband electromagnetic waves and manipulation of thermal conditions on the surface of an object and believe that multiband camouflage and thermal management can be used for diverse applications in the military industry.

4. EXPERIMENTAL SECTION

A. Fabrication of Wavelength-Selective Emitter

Ge/YbF_3 multilayers were deposited on silicon substrates by electron-beam evaporation at rates of 0.5 (Ge) and 1 nm/s (YbF_3).

B. Emittance/Absorptance Spectrum Measurements

For the visible section, the reflectance at wavelengths of 380–780 nm was measured using a spectrophotometer (Shanghai Jinghua 723PC). For the mid-IR section, Fourier-transform IR (Vertex 70, Brucker) and DTGS/MCT detectors were used to measure the emissivity/absorption.

C. Apparent Temperature Measurements

The radiation temperature was measured using an IR camera (HM-TP76-25SVF/W, HIKMICRO) for mid-wavelength IR in the 3–5 μm range and long-wavelength IR in the 8–14 μm range. The surface temperature was measured using thermocouples (5TC-TT-K30-36, Omega) and a digital acquisition box (H300C, Hong Run Instruments). The thermocouples were attached to the upper surface of samples I (wavelength-selective emitter on silica aerogel), II (titanium alloy on silica aerogel), and III (exposed silica aerogel).

D. Simulations

Simulations were performed using the finite-difference time-domain solver of Lumerical Solutions (version 8.13). The optical constants of germanium and titanium alloys were obtained from Refs. [48,49], respectively. The relative permittivity of YbF_3 was obtained empirically by IR ellipsometry, as described in Appendix A (as shown in Fig. 8). According to Kirchhoff's law of thermal radiation, we considered that the simulated emissivity can be replaced by the simulated absorptivity, and the observed angle can be replaced by the incidence angle.

APPENDIX A: OPTICAL CONSTANTS OF YbF_3

The optical constants (refractive index n, extinction coefficient k) of YbF_3 were measured by an infrared ellipsometer.

APPENDIX B: TEMPERATURE ENDURANCE AND FILM STRENGTH

The emission spectra of Ge/YbF_3 multilayers before heating (blue dashed line) and after heating at 623 K for 1 h (orange dashed line) are basically the same (Fig. 9), indicating the strong temperature tolerance of the designed multilayer structure. No delamination occurred after heating at 623 K for 1 h,

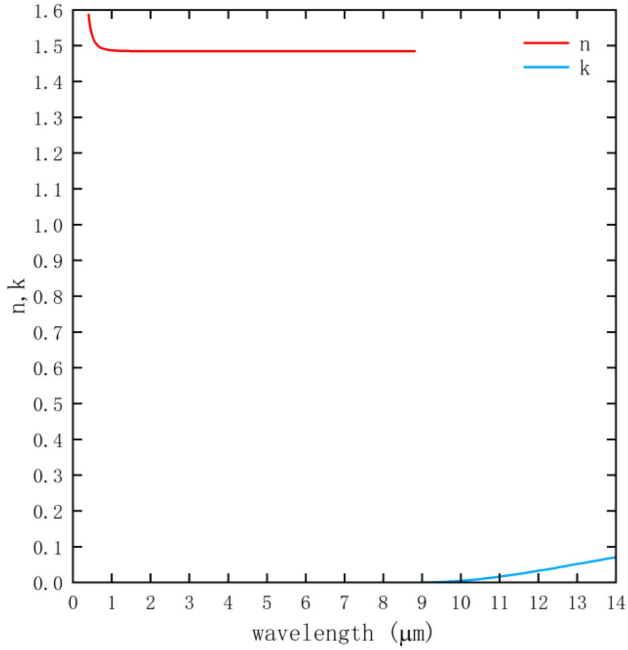

Fig. 8. Refractive index n and extinction coefficient k of YbF_3.

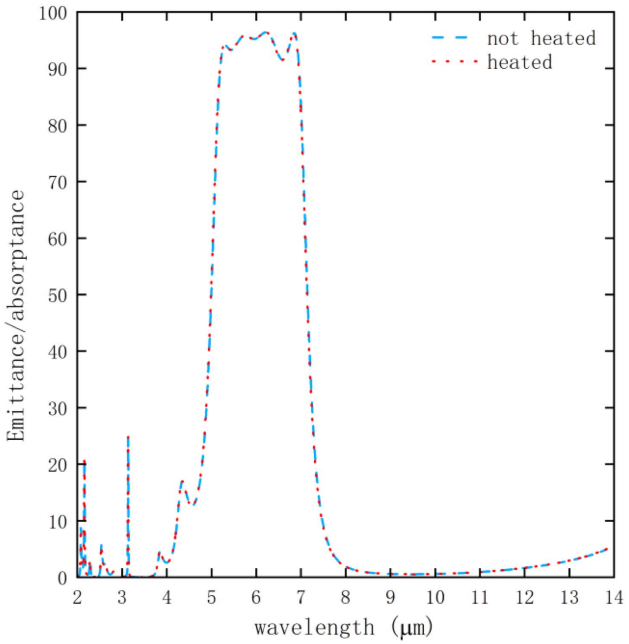

Fig. 9. Emission spectra of multilayers before heating (blue dashed line) and after heating at 623 K for 1 h (orange dashed line).

indicating the strong membrane strength of the designed multilayer structure. The data in Fig. 9 were obtained from our experiments and are not cited from other literature.

Funding. National Key Research and Development Program of China (2021YFC2202103, 2021YFC2202203); National Natural Science Foundation of China (12103081, 42101380, 61875257).

Disclosures. The authors declare no conflicts of interest.

Data Availability. Data underlying the results presented in this paper are not publicly available at this time but may be obtained from the authors upon reasonable request.

REFERENCES

1. Y. Li, X. Bai, T. Yang, H. Luo, and C.-W. Qiu, "Structured thermal surface for radiative camouflage," Nat. Commun. **9**, 273 (2018).
2. O. Ilic, P. Bermel, G. Chen, J. D. Joannopoulos, I. Celanovic, and M. Soljacic, "Tailoring high-temperature radiation and the resurrection of the incandescent source," Nat. Nanotechnol. **11**, 320–324 (2016).
3. B. W. Bai, X. P. Li, J. Xu, and Y. M. Liu, "Reflections of electromagnetic waves obliquely incident on a multilayer stealth structure with plasma and radar absorbing material," IEEE Trans. Plasma Sci. **43**, 2588–2597 (2015).
4. K. Iwaszczuk, A. C. Strikwerda, K. Fan, X. Zhang, R. D. Averitt, and P. U. Jepsen, "Flexible metamaterial absorbers for stealth applications at terahertz frequencies," Opt. Express **20**, 635–643 (2012).
5. L. Zhao, H. Liu, Z. He, and S. Dong, "All-metal frequency-selective absorber/emitter for laser stealth and infrared stealth," Appl. Opt. **57**, 1757–1764 (2018).
6. Y. Huang, M. Pu, Z. Zhao, X. Li, X. Ma, and X. Luo, "Broadband metamaterial as an 'invisible' radiative cooling coat," Opt. Commun. **407**, 204–207 (2018).
7. H. Hogstrom, G. Forssell, and C. G. Ribbing, "Realization of selective low emittance in both thermal atmospheric windows," Opt. Eng. **44**, 026001 (2005).
8. C. Xu, S. Qu, Y. Pang, J. Wang, M. Yan, J. Zhang, Z. Wang, and W. Wang, "Metamaterial absorber for frequency selective thermal radiation," Infrared Phys. Technol. **88**, 133–138 (2018).
9. T. Yang, X. Bai, D. Gao, L. Wu, B. Li, J. T. L. Thong, and C.-W. Qiu, "Invisible sensors: simultaneous sensing and camouflaging in multiphysical fields," Adv. Mater. **27**, 7752–7758 (2015).
10. T. Han, X. Bai, J. T. L. Thong, B. Li, and C.-W. Qiu, "Full control and manipulation of heat signatures: cloaking, camouflage and thermal metamaterials," Adv. Mater. **26**, 1731–1734 (2014).
11. J. Kim, K. Han, and J. W. Hahn, "Selective dual-band metamaterial perfect absorber for infrared stealth technology," Sci. Rep. **7**, 6740 (2017).
12. D. Liu, H. Ji, R. Peng, H. Cheng, and C. Zhang, "Infrared chameleon-like behavior from VO_2(M) thin films prepared by transformation of metastable VO_2(B) for adaptive camouflage in both thermal atmospheric windows," Sol. Energy Mater. Sol. Cells **185**, 210–217 (2018).
13. W. Wang, L. Zhang, S. Fang, H. Xu, Y. Zhong, and Z. Mao, "Low-emitting property of lanthanum aluminate and its application in infrared stealth," Sci. Adv. Mater. **7**, 1649–1656 (2015).
14. A. P. Raman, M. A. Anoma, L. Zhu, E. Rephaeli, and S. Fan, "Passive radiative cooling below ambient air temperature under direct sunlight," Nature **515**, 540–544 (2014).
15. B. Bhatia, A. Leroy, Y. Shen, L. Zhao, M. Gianello, D. Li, T. Gu, J. Hu, M. Soljacic, and E. N. Wang, "Passive directional sub-ambient daytime radiative cooling," Nat. Commun. **9**, 5001 (2018).
16. T. Li, Y. Zhai, S. M. He, W. T. Gan, Z. Y. Wei, M. Heidarinejad, D. Dalgo, R. Y. Mi, X. P. Zhao, J. W. Song, J. Q. Dai, C. J. Chen, A. Aili, A. Vellore, A. Martini, R. G. Yang, J. Srebric, X. B. Yin, and L. B. Hu, "A radiative cooling structural material," Science **364**, 760–763 (2019).
17. P. C. Hsu, A. Y. Song, P. B. Catrysse, C. Liu, Y. C. Peng, J. Xie, S. H. Fan, and Y. Cui, "Radiative human body cooling by nanoporous polyethylene textile," Science **353**, 1019–1023 (2016).
18. X. Xie, X. Li, M. Pu, X. Ma, K. Liu, Y. Guo, and X. Luo, "Plasmonic metasurfaces for simultaneous thermal infrared invisibility and holographic illusion," Adv. Funct. Mater. **28**, 1706673 (2018).
19. C. Xu, G. T. Stiubianu, and A. A. Gorodetsky, "Adaptive infrared-reflecting systems inspired by cephalopods," Science **359**, 1495–1500 (2018).
20. L. Xiao, H. Ma, J. Liu, W. Zhao, Y. Jia, Q. Zhao, K. Liu, Y. Wu, Y. Wei, S. Fan, and K. Jiang, "Fast adaptive thermal camouflage based on flexible VO_2/graphene/CNT thin film," Nano Lett. **15**, 8365–8370 (2015).
21. Y. Qu, Q. Li, L. Cai, M. Pan, P. Ghosh, K. Du, and M. Qiu, "Thermal camouflage based on the phase-changing material GST," Light Sci. Appl. **7**, 26 (2018).
22. K. K. Du, Q. Li, Y. B. Lyu, J. Ding, Y. Lu, Z. Cheng, and M. Qiu, "Control over emissivity of zero-static-power thermal emitters based on phase-changing material GST," Light Sci. Appl. **6**, e16194 (2017).
23. Y. Qu, Q. Li, K. Du, L. Cai, J. Lu, and M. Qiu, "Dynamic thermal emission control based on ultrathin plasmonic metamaterials including phase-changing material GST," Laser Photonics Rev. **11**, 1700091 (2017).
24. M. J. Moghimi, G. Lin, and H. Jiang, "Broadband and ultrathin infrared stealth sheets," Adv. Eng. Mater. **20**, 1800038 (2018).
25. X. Ye, Y. Zhou, Y. Sun, J. Chen, and Z. Wang, "Structure and infrared emissivity of collagen/SiO_2 composite," Appl. Surf. Sci. **254**, 5975–5980 (2008).
26. Z. Wang, Y. Zhou, and Y. Sun, "Preparation, characterization and infrared emissivity study of Attapulgite@helical polyurethane composites," J. Inorg. Organomet. Polym. **19**, 202–207 (2009).
27. X. Bu, Y. Zhou, M. He, Z. Chen, and T. Zhang, "Optically active SiO_2/TiO_2/polyacetylene multilayered nanospheres: preparation, characterization, and application for low infrared emissivity," Appl. Surf. Sci. **288**, 444–451 (2014).
28. C. Zhang, J. Yang, W. Yuan, J. Zhao, J. Y. Dai, T. C. Guo, J. Liang, G. Y. Xu, Q. Cheng, and T. J. Cui, "An ultralight and thin metasurface for radar-infrared bi-stealth applications," J. Phys. D **50**, 444002 (2017).

29. C. Zhang, X. Wu, C. Huang, J. Peng, C. Ji, J. Yang, Y. Huang, Y. Guo, and X. Luo, "Metamaterials: flexible and transparent microwave–infrared bistealth structure," Adv. Mater. Technol. **4**, 1900063 (2019).
30. S. Chandra, D. Franklin, J. Cozart, A. Safaei, and D. Chanda, "Adaptive multispectral infrared camouflage," ACS Photonics **5**, 4513–4519 (2018).
31. B. Liu, J. M. Shi, J. K. Zhang, Z. G. Li, Z. S. Chen, and X. S. Deng, "Infrared stealth performance analysis of photonic crystal with high heat dissipation," Opt. Mater. **111**, 110689 (2021).
32. H. Zhu, Q. Li, C. Tao, Y. Hong, Z. Xu, W. Shen, S. Kaur, P. Ghosh, and M. Qiu, "Multispectral camouflage for infrared, visible, lasers and microwave with radiative cooling," Nat. Commun. **12**, 1805 (2021).
33. W. Zhang, G. Xu, J. Zhang, H. Wang, and H. Hou, "Infrared spectrally selective low emissivity from Ge/ZnS one-dimensional heterostructure photonic crystal," Opt. Mater. **37**, 343–346 (2014).
34. T. Kim, J.-Y. Bae, N. Lee, and H. H. Cho, "Hierarchical metamaterials for multispectral camouflage of infrared and microwaves," Adv. Funct. Mater. **29**, 1807319 (2019).
35. B. Vasić and R. Gajić, "Graphene induced spectral tuning of metamaterial absorbers at mid-infrared frequencies," Appl. Phys. Lett. **103**, 261111 (2013).
36. H. Zhu, Q. Li, C. Zheng, Y. Hong, Z. Xu, H. Wang, W. Shen, S. Kaur, P. Ghosh, and M. Qiu, "High-temperature infrared camouflage with efficient thermal management," Light Sci. Appl. **9**, 60 (2020).
37. L. Peng, D. Liu, H. Cheng, S. Zhou, and M. Zu, "A multilayer film based selective thermal emitter for infrared stealth technology," Adv. Opt. Mater. **6**, 1801006 (2018).
38. M. Pan, Y. Huang, Q. Li, H. Luo, H. Zhu, S. Kaur, and M. Qiu, "Multiband middle-infrared-compatible camouflage with thermal management via simple photonic structures," Nano Energy **69**, 104449 (2020).
39. L. Wang, Y. Yang, X. Tang, B. Li, Y. Hu, Y. Zhu, and H. Yang, "Combined multi-band infrared camouflage and thermal management via a simple multilayer structure design," Opt. Lett. **46**, 5224–5227 (2021).
40. Y. Cui, K. H. Fung, J. Xu, H. Ma, Y. Jin, S. He, and N. X. Fang, "Ultrabroadband light absorption by a sawtooth anisotropic metamaterial slab," Nano Lett. **12**, 1443–1447 (2012).
41. E. Maciá, "Thermal emission control via bandgap engineering in aperiodically designed nanophotonic devices," Nanomaterials **5**, 814–825 (2015).
42. M. Pu, C. Hu, M. Wang, C. Huang, Z. Zhao, C. Wang, Q. Feng, and X. Luo, "Design principles for infrared wide-angle perfect absorber based on plasmonic structure," Opt. Express **19**, 17413–17420 (2011).
43. N. Bheekhun, A. R. A. Talib, and M. R. Hassan, "Aerogels in aerospace: an overview," Adv. Mater. Sci. Eng. **2013**, 406065 (2013).
44. Z.-H. Ruan, Y. Yuan, X.-X. Zhang, Y. Shuai, and H.-P. Tan, "Determination of optical properties and thickness of optical thin film using stochastic particle swarm optimization," Solar Energy **127**, 147–158 (2016).
45. Y.-M. Liu, G.-J. Chai, X.-H. Wang, and B.-L. Zhang, "Visible characteristics and calculation of detecting distance for space target," Infrared Technol. **31**, 23–26 (2009).
46. J. M. Luque-Raigon, J. Halme, and H. Miguez, "Fully stable numerical calculations for finite one-dimensional structures: mapping the transfer matrix method," J. Quant. Spectrosc. Radiat. Transfer **134**, 9–20 (2014).
47. G. A. Rao and S. P. Mahulikar, "Aircraft powerplant and plume infrared signature modelling and analysis," in *43rd AIAA Aerospace Sciences Meeting and Exhibit AIAA* (2005), paper AIAA 2005-221.
48. E. D. Palik, ed. *Handbook of Optical Constants of Solids* (Academic, 1997), pp. 465–478.
49. Z. Wenjie, "Experimental study on high temperature optical constants of typical engineering materials based on ellipsometry," Ph.D. dissertation (Harbin Institute of Technology, 2015).